Phase-retrieval Fourier microscopy of partially temporally coherent nanoantenna radiation patterns

NICK J. SCHILDER,[1] Tom A. W. WOLTERINK,[1] CHRISTIAAN MENNES,[1] RUSLAN RÖHRICH,[1,2] AND A. FEMIUS KOENDERINK[1,*]

[1]*Center for Nanophotonics, AMOLF, Science Park 104, 1098 XG Amsterdam, The Netherlands*
[2]*Advanced Research Center for Nanolithography, Science Park 106, 1098 XG Amsterdam, The Netherlands*
[*]*f.koenderink@amolf.nl*

Abstract: We report an experimental technique for determining phase-resolved radiation patterns of single nanoantennas by phase-retrieval defocused imaging. A key property of nanoantennas is their ability to imprint spatial coherence, for instance, on fluorescent sources. Yet, measuring emitted wavefronts in absence of a reference field is difficult. We realize a defocused back focal plane microscope to measure phase even for partially temporally coherent light and benchmark the method using plasmonic bullseye antenna scattering. We outline the limitations of defocused imaging which are set by spectral bandwidth and antenna mode structure. This work is a first step to resolve wavefronts from fluorescence controlled by nanoantennas.

1. Introduction

In the fields of metasurfaces and plasmonics, a precise understanding and control of resonant multipolar scattering by nanoscale objects into the far field is crucial. For instance, metasurfaces are built up from high-index dielectric nanoparticles or plasmonic antennas and reshape impinging wavefronts upon reflection and transmission by virtue of the fact that each scatterer has a controlled scattering phase, amplitude, and polarization characteristic [1–3]. Placing such resonant nanoscatterers in oligomers [4–6] or lattices [7,8] gives rise to a plethora of phenomena due to multipolar far field interference. These include spectral signatures, such as Fano resonances [9], as well as strong directional scattering (Huygens and Kerker phenomena), chiroptical scattering effects [10,11], the exchange of orbital angular momentum, and the interconversion of spin and orbital angular momentum [12–15]. Beyond the context of scattering, these phenomena also deeply impact near-to-far field transformations. For instance, nanoscale antennas have been shown to allow the precise tailoring of the radiation pattern of single fluorophores [16]. While single fluorescent emitters are by themselves dipolar point sources, coupling them to the resonant modes of nanophotonic structures can impart significant directivity, as well as funneling of radiation into preferred polarization channels. Seminal examples are the plasmonic Yagi-Uda phased array antenna [17,18], plasmonic lattices to shape emission by surface lattice resonances [19,20], and metal nano-aperture antennas for solution-phase fluorescent microscopy developed by Aouani *et al*. [21,22].

Fourier microscopy has become the method of choice to quantify the multipolar and directional scattering properties of antennas and fluorescent nanosources [23–25]. Fourier microscopy can be performed in a conventional high-NA microscope by placing a spatial filter confocal with the nano-object of choice in the detection path, followed by a 'Bertrand' or Fourier-transform lens to ensure that the camera detector does not image the sample, but the objective back focal plane. For a full mapping of radiation patterns, one ideally records amplitude, phase, and polarization for each angle in 4π sr. In practice, the state of the art is mapping with sub-1° resolution within

the collection of NA's up to 0.95, and with full polarimetric resolution by Stokes polarimetry [26,27]. Recently, digital holographic methods have been applied to nanoantenna scattering to achieve phase resolution [28].

Interferometric methods to resolve phase in Fourier microscopy require a spatially and temporally coherent reference beam and are therefore only feasible for laser scattering experiments. This should be contrasted to the needs of experiments, where nanoantennas are used to control spontaneous photon emission. As an extreme scenario, it should be in principle possible to, e.g., even impart orbital angular momentum to the stream of single photons emitted by a fluorophore coupled to spiral versions of the bullseye antenna reported by Aouani *et al.* [21,22]. While no absolute phase reference is available or even sensible for a stream of single photons, each single photon could nonetheless be emitted with a spiraling wavefront that should be visible in *self-interference* experiments [29]. Fully capturing such partially coherent wavefronts of nanoscale single emitters shaped by complex nanophotonic metasurfaces in amplitude, polarization, and phase is still an outstanding challenge in nanophotonics. There is thus a need for a reference-free imaging technique that is able to resolve phase maps in radiation patterns of single nano-objects. Even in less demanding contexts this capability would be of use, i.e., in scattering experiments with only partially coherent excitation, and modification of coherence by the nanophotonic structure.

Here we explore defocused imaging with algorithmic phase retrieval as a technique to obtain quantitative phase information relevant to far field scattering patterns of single nano-objects, combining Fourier microscopy with phase-resolved defocused imaging and partially temporally coherent light. Defocused imaging is known in real space imaging [30,31] as a technique that is robust against partial coherence and requires a relatively simple setup [32–35]. Examples of other quantitative phase imaging techniques that are robust under partially coherent illumination are digital holography [36,37], self-interference techniques [38], such as optical scanning holography [39], Fresnel incoherent correlation holography [40], and self-interference incoherent digital holography [41], transport-of-intensity equation methods [42], and iterative phase retrieval techniques, such as coherent diffraction imaging, mixed-state ptychography [43], and defocused imaging as explored in this work. Yet, common digital holography methods rely on the presence of a reference beam and mixed-state ptychography is incompatible with fluorescence microscopy. Self-interference methods do enable fluorescence imaging, but iterative defocused imaging techniques benefit from less complex setups and lower detection requirements, e.g. in dynamic range, due to the absence of interference. Of the non-interferometric approaches, transport-of-intensity equation methods offer faster reconstruction of the field with guaranteed convergence, while in iterative methods the reconstruction can be aided by a-priori known constraints to boost their performance. A challenge for defocused imaging techniques that leads to phase ambiguities is the presence of intensity zeros [32,34]. In nanophotonic applications, such intensity zeros associated with phase singularities can occur even for relatively simple nanostructure designs [1,28,44]. One can deal with the presence of phase singularities by using many defocused images [34] or by providing proper boundary conditions to the iterative retrieval algorithm [35].

In this work, we present the first step towards phase-resolved Fourier microscopy without a reference beam. To this end, we experimentally study phase retrieval in elastic scattering experiments on an individual plasmonic bullseye antenna by illuminating with partially temporally coherent light. Figure 1 presents a schematic view of the concept of phase retrieval based on defocused Fourier imaging. With a conventional Fourier microscope we image the angular scattering profile. We then move the camera to obtain defocused images of the back focal plane of the objective. These defocused images serve as input to an iterative phase retrieval algorithm that retrieves the angle-dependent phase of the scattered electric field. We combine single nanoantenna Fourier microscopy with algorithmic phase retrieval as is already commonly used for reconstruction in real-space imaging of weakly scattering objects [45]. This paper is

organized as follows. First, we benchmark the iterative algorithm phase retrieval by defocused Fourier imaging against off-axis digital holography for highly temporally coherent light coming from a HeNe laser. Next, we reduce the temporal coherence significantly, by using a spectrally filtered supercontinuum laser with a bandwidth of 1 nm and verify if the iterative algorithm is still able to retrieve phase. Finally, we extend the bandwidth of the incident field such that the optical response of the bullseye antenna becomes dispersive to probe the limits of defocused imaging. This work leads to the introduction of two criteria on the temporal coherence properties required for phase-resolved Fourier microscopy by defocused imaging.
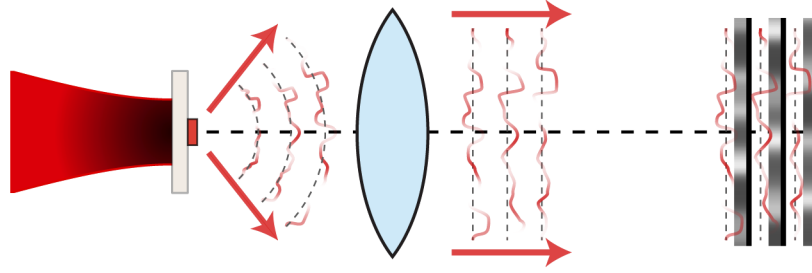

Fig. 1. Schematic of phase-resolved Fourier microscopy without a reference beam. A nanoscale structure radiates a spherical wave with a characteristic phase and amplitude profile, which is transformed into a plane wave in the objective's back focal plane. Measuring the intensity of the far field scattering profile at different distances, providing a series of defocused images of the back focal plane, enables the reconstruction of the phase of the far field scattering profile through an iterative algorithm.

2.   Phase-retrieval Fourier microscopy setup and algorithm

The key idea of this work is demonstrated in Fig. 1. We envision a nanoscale structure that radiates its scattered field as a spherical wave $\mathbf{S}(\theta, \varphi)\frac{e^{ikr}}{r}$ into a microscope objective. The goal is to quantify the complex-valued amplitude function $\mathbf{S}(\theta, \varphi)$ that depends on the zenithal angle θ relative to the optical axis and the azimuthal angle φ. The idea of standard Fourier microscopy is that the objective's back focal plane is imaged onto a camera plane to obtain a sharp image of $|\mathbf{S}|^2$. The main point of this work is to retrieve the far field scattering phase profile $\phi = \arg(\mathbf{S})$ by an iterative algorithm from a series of defocused far field scattering intensity profiles.

Figure 2(a) shows a schematic of the experimental setup for defocused Fourier imaging. We illuminate a single scattering object with a weakly focused beam ($f = 125$ mm lens). Transmitted light is collected by an objective (NA = 0.8, 50× Nikon CFI Plan Fluor BD). To collect only light scattered by a single scattering object, we place a 300 μm circular pinhole in the middle of a 1:1 telescope ($2f_{telescope} = 100$ mm). This configuration leads to a circular collection area of 24 μm. After the 1:1 telescope, we place both a Fourier lens (FL, $f_{FL} = 200$ mm) and a tube lens (TL, $f_{TL} = 80$ mm) to make the back focal planes (BFP) of the objective and the tube lens conjugate planes. The BFP of the tube lens is the plane $\Delta z = 0$ cm. For defocused imaging, we translate the CCD camera in steps of 1 cm over a distance of 25 cm. To analyze polarization states, we place a quarter-wave plate (QWP$_2$) and a linear polarizer (LP$_2$) between the FL and the TL. We define the polarization state from the perspective of the detector. In this work we use two different light sources: a HeNe laser ($\lambda = 632.8$ nm) for high temporal coherence illumination, and a filtered supercontinuum laser for partially temporal coherence.

Figure 3 shows a schematic of the phase retrieval numerical algorithm. This algorithm was first proposed in the field of electron microscopy [45]. For the schematic we apply the algorithm to a simulated Gaussian beam for which the plane $\Delta z = 0$ cm is placed behind the focus, so that
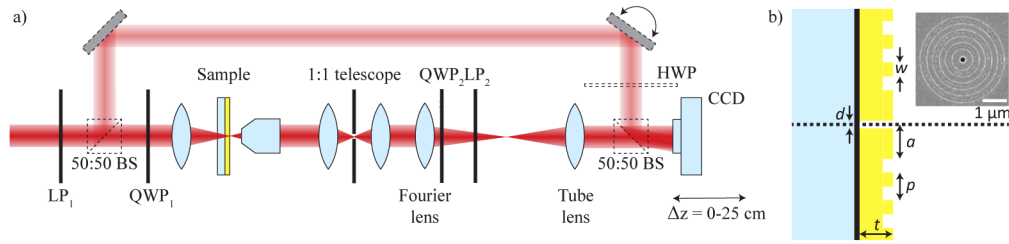
Fig. 2. Schematic of setup. (a) Fourier polarimetry setup, consisting of a transmission microscope. The microscope contains a 1:1 telescope with a pinhole in between for spatial filtering of light from a single bullseye antenna. A Fourier lens and tube lens (TL) image the back focal plane of the objective. The detector plane (CCD) is translated over a range of 25 cm to perform defocused Fourier imaging. Dashed optical elements are used for holography experiments only. (b) Schematic view of the bullseye antenna. Inset shows an SEM image of a bullseye antenna.

the phase profile is nontrivial. To start the iterative retrieval an initial guess of the electric field in the plane $\Delta z = 0$ cm is required. The initial amplitude of the field is obtained simply from the measured intensity in the plane $\Delta z = 0$ cm. The initial guess of the phase in this work is either taken as random uniformly distributed with a range of $\pi/5$ around a uniform phase, or a phase gradient, unless stated differently. The phase gradient captures the trivial linear translation of the image that in case of small setup misalignments is observed as the camera is moved along the optical axis. The next step in the algorithm is to numerically propagate the initial electric field to the different planes in which intensity measurements have been performed. To this end we perform a plane wave decomposition of the electric field in the plane $\Delta z = 0$ cm $[E_{\Delta z=0}(x_{\text{CCD}}, y_{\text{CCD}})]$ by means of a 2D Fast Fourier transform $[\tilde{E}_{\Delta z=0}(k_x, k_y)]$, where the tilde indicates that the quantity has been Fourier transformed. For numerical propagation of the field to
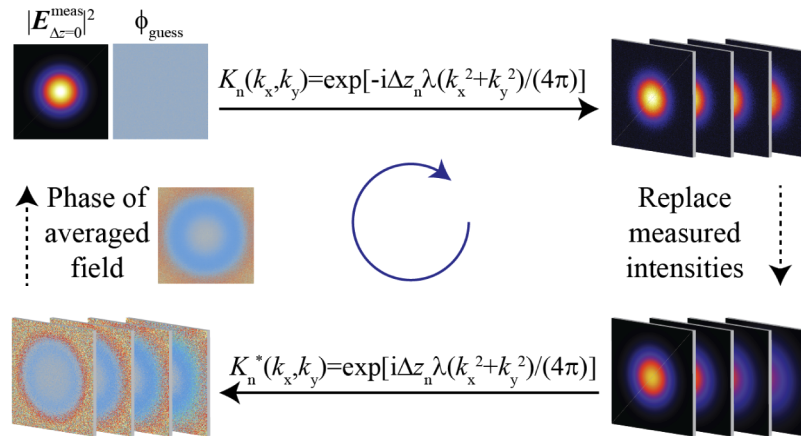
Fig. 3. Protocol used for iterative phase retrieval by defocused Fourier imaging. The iterative algorithm has as input the measured intensity in N planes and a guess for the phase profile in the plane $\Delta z = 0$ cm. Numerical propagation to N planes is done within the paraxial beam approximation. Replacing the obtained intensity profiles with measured intensity profiles, the complex fields are simultaneously backpropagated to the initial plane. The phase profile of the averaged electric field serves as input for the next iteration. This process is repeated until convergence.

the nth plane we use $\tilde{E}_n(k_x, k_y) = K_n(k_x, k_y; \Delta z_n)\tilde{E}_{\Delta z=0}(k_x, k_y)$, where the propagator K_n is, within the paraxial beam approximation, given by

$$K_n(k_x, k_y; \Delta z_n) = \exp[-i\Delta z_n \lambda (k_x^2 + k_y^2)/(4\pi)]. \tag{1}$$

The electric fields in the detector planes for defocused imaging are obtained by the inverse 2D Fast Fourier transform. The next step in the algorithm is to replace the amplitudes of the fields by the measured amplitudes while retaining the phase calculated previously, and numerically backpropagating to the plane $\Delta z = 0$ cm. The result is used to define the input field for the next iteration: again the amplitude is taken as the measured amplitude, but the phase profile is taken as the arithmetic mean of the fields backpropagated from all the detector planes. This process is repeated until the retrieved electric field has converged. From the retrieved electric field we extract the phase distribution. Finally, it is necessary to convert the camera spatial coordinates $(x_{\text{CCD}}, y_{\text{CCD}})$ into the angles θ, φ in the radiation pattern, or equivalently $(x_{\text{CCD}}, y_{\text{CCD}}) \mapsto (k_x/k_0, k_y/k_0)$ with $(k_x, k_y) = k_0(\cos\varphi\sin\theta, \sin\varphi\sin\theta)$. The calibration for this coordinate transformation was verified by imaging the diffraction pattern of a 2D grating for which the period is known.

3. Scattering geometry

We choose plasmonic bullseye antennas milled in gold as structures on which to test phase-retrieval Fourier microscopy. This choice is motivated by the fact that it provides significant and well-understood directionality [26,46,47], that it blocks the incident beam from directly reaching the detector, and by the fact that bullseyes display a conversion in (orbital angular momentum) phase content upon scattering that is well understood via spin and OAM selection rules [12,28]. Their well-understood nontrivial radiation patterns make plasmonic bullseye antennas suitable for benchmarking our phase-retrieval technique. Figure 2(b) shows a schematic view of the cross section of the bullseye antenna. The inset shows a scanning electron microscope image of a typical bullseye antenna. The bullseye antenna was fabricated by first depositing a 5-nm-thin Cr film on a glass substrate using electron-beam evaporation. Subsequently, a $t = 200$ nm Au film was deposited using electron-beam evaporation. The Cr film serves both to prevent exciting surface plasmon polaritons (SPP) at the glass/Au interface and to promote adhesion and homogeneity of the Au film. Focused ion-beam milling using 30 keV Ga ions was used to define bullseye antennas. The results that we present were obtained on a bullseye antenna consisting of three concentric grooves with a period $p = 520$ nm, a duty cycle of 50 %, and a depth of 60 nm. The first groove starts at a radial distance $a = 440$ nm from the center of the bullseye. At the center of the bullseye is a hole with a diameter $d = 200$ nm.

The expected salient scattering properties of plasmonic bullseye antennas are illustrated by Fig. 4, which summarizes simulations based on a modal method for diffraction of light by finite cylindrically symmetric objects [48]. For the simulations we consider the precise optical setup as used in the experiment, including all optical elements shown in Fig. 2(a) along the optical axis after the sample. The refractive indices for both Cr and Au are taken from Johnson and Christy [49]. The refractive index of the substrate is taken as 1.5. Figures 4(a) and (b) show the predicted angular scattering pattern, respectively angular phase profile, of our bullseye antenna illuminated with a vertically polarized plane wave, assuming also vertically polarized detection. We show the angular scattering patterns for three salient wavelengths ($\lambda = \{582.8, 632.8, 682.8\}$ nm) chosen for experiments in this work, at and below the 2nd order Bragg diffraction expected for a grating of pitch p. These three nearby wavelengths are chosen because light scattering is significantly different particularly regarding the variation of the phase as a function of wavelength, allowing us to meaningfully test phase retrieval as a function of the bandwidth of the offered light relative to the frequency spectrum of the structure. We note that the radiation patterns generally consist of a broad, homogeneous background from the scattering of the center hole of the bullseye antenna,

interfering with a more strongly directional beam that is due to outcoupling of surface plasmon polaritons by the grooves [26,28,46,47,50].

Figure 4(c) shows a frequency-wavevector cross cut of the angular scattering patterns presented in Fig. 4(a) along the line $k_x/k_0 = 0$ for a wavelength range from 400 to 900 nm in steps of 5 nm.
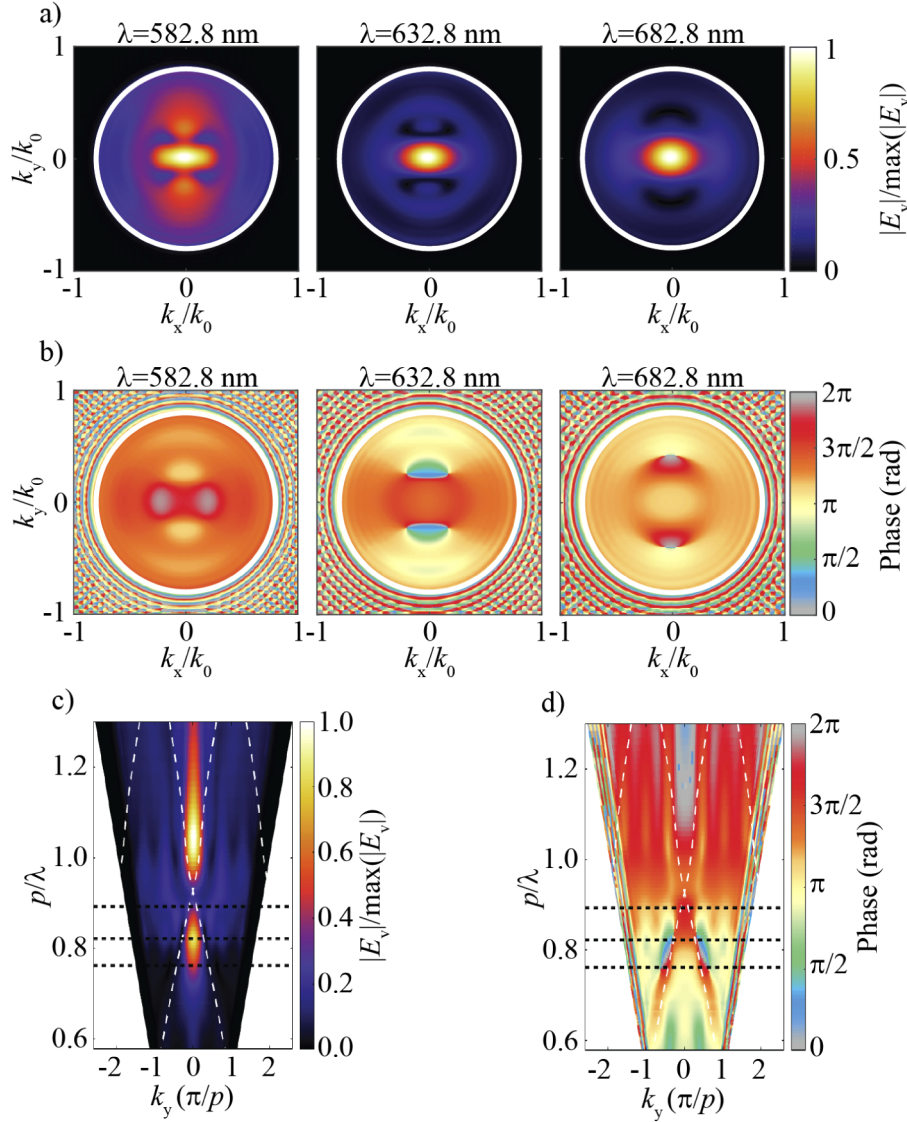

Fig. 4. Calculated wavelength and momentum-resolved bullseye antenna scattering. (a,b) Numerically calculated angular scattering pattern (a) and angular phase profile (b) for a bullseye antenna with period $p = 520$ nm illuminated by a plane wave for $\lambda = \{582.8, 632.8, 682.5\}$ nm. (c,d) Numerically calculated scattered intensity (c) and phase (d) as a function of p/λ and k_y for a bullseye antenna with a fixed period ($p = 520$ nm) and varying wavelength at $k_x = 0$. The white dashed curves indicate calculated dispersion relation for a 1D grating ($p = 520$ nm). Black dashed lines indicate the wavelengths used in the experiments: $\lambda \in \{582.8, 632.8, 682.8\}$ nm. (a-d) A vertically polarized plane wave is incident on the bullseye antenna and vertically polarized light is detected.

We fixed the period to $p = 520$ nm. We observe forward beaming for a broad range of wavelengths. Even though we have a diffractive element, there are no angles with identically zero intensity. The 200-nm-diameter nanohole at the center of the bullseye scatters light over a broad range of wavelengths and angles with an amplitude comparable to the scattered SPPs from the grooves. The SPPs launched at the hole scatter directionally since they essentially form a cylindrical TM polarized wave of definite momentum k_{SPP} that is outcoupled by Bragg diffraction at the grooves. As guides to the eye, white dashed curves indicate the folded-free-photon dispersion relation for a 1D grating, including the dispersive propagation of SPPs on a vacuum/Au interface. Dominant features in the diffraction occur near the band crossing (2nd order Bragg condition) in this dispersion relation. Nonetheless, the intensity profile does not trace the white dashed curves. We attribute this to the fact that (a) the structure is cylindrical and not 1D periodic, (b) the intensity profile is the result not of the SPPs alone, but interference with the strong contribution of the nanohole, and (c) the break in periodicity close to the origin, whereby the precise position of the *first* groove relative to the hole matters, and not just the groove pitch. In scattered phase (Fig. 4(d)) the folded SPP dispersion is more evident. In Figs. 4(c) and (d) black horizontal lines indicate the three wavelengths ($\lambda = \{582.8, 632.8, 682.8\}$ nm) chosen for experiments in this work.

4. Coherent Fourier microscopy experiment: phase retrieval versus interferometry

To demonstrate phase-resolved Fourier microscopy by defocused imaging, we first shine vertically polarized light from a HeNe laser onto a bullseye antenna. We detect left-hand circular (LHC) polarized light. Figure 5(a) shows the measured electric field amplitude. A close-to-horizontally oriented lobe is observed for forward scattering angles. Off-normal, we observe that both intensity maxima and minima follow an s-shape, the minima being interrupted by the lobe for forward scattering angles. Figure 5(b) shows the retrieved phase profile. The retrieved phase profile is close to uniform and shows two patches for $k_r/k_0 \approx 0.25$. These patches have a phase shift close to $\pi/2$ as compared to the uniform background. To verify the retrieved phase, we benchmark the defocussed imaging results against well-established off-axis digital holography. To perform off-axis digital holography, we add two 50:50 beamsplitters (BS), two mirrors, and a half-wave plate (HWP) [28]. The HWP is used to rotate the polarization of the reference field to be parallel with the detected linear polarization of the signal field. Refer to Fig. 2(a) for this setup. The overlap between the retrieved fields from off-axis digital holography ($\mathbf{E}_{hol}$, Figs. 5(c) and (d)) and from defocused imaging ($\mathbf{E}_{defoc}$) $| \int \mathbf{E}_{hol} \cdot \mathbf{E}_{defoc}^* dk_x dk_y |^2 / \left[\int |\mathbf{E}_{hol}|^2 dk_x dk_y \int |\mathbf{E}_{defoc}|^2 dk_x dk_y \right] = 0.97$. This agreement shows that defocused imaging can indeed be used for Fourier microscopy on single scattering objects.

Figure 6(a) presents the simulated scattered field. These results show resemblance with the experimentally obtained scattered fields. The simulation shows a horizontally oriented main lobe in the origin. The experimental data shows a minor rotation of this main lobe, which we attribute to both the dispersion present in our achromatic QWP$_2$ and a minor misalignment of QWP$_2$. The simulated phase profile shows, similar to our experimentally retrieved phase profile, two patches. In the simulation, each patch contains both a phase singularity of topological charge +1 and -1. We do not observe these phase singularities in our experimental data at the HeNe wavelength. A potential cause of the absence of phase singularities in the experiment is that the scattered field from the hole appears to be stronger relative to the scattered field from the grooves in the experiment than in theory, likely due to a mismatch in geometry between simulation and fabricated object. Based on simulations, we understand that the nanohole itself radiates a close-to-spherical uniform wavefront. For the angles at which we observe patches, scattered
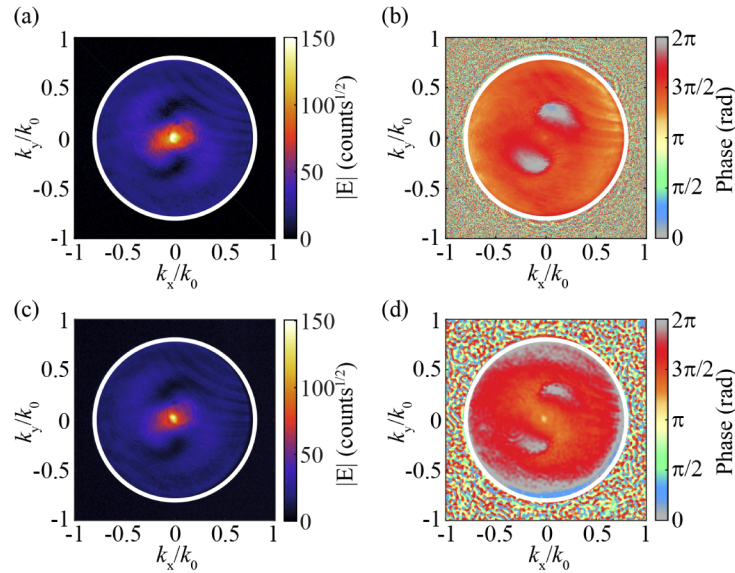
Fig. 5. Recovered electric far field from bullseye antenna. (a) Measured electric field amplitude for defocused imaging experiment. (b) Phase of the electric field obtained by defocused imaging. (c) Measured electric field amplitude for off-axis digital holography experiment. (d) Phase of the electric field obtained by off-axis digital holography experiment. (a-d) Vertically polarized HeNe laser ($\lambda = 632.8$ nm) is incident on the bullseye antenna and left-hand circularly polarized light is analyzed.

SPPs by the grooves are stronger than light scattered from the nanohole, deviating thereby from a close to spherical wavefront.

To focus on a radiation pattern with a richer phase structure we turn to crossed circular polarization. In exactly crossed circular polarization one would expect an OAM content of ±2, as a consequence of spin-OAM conversion [12,28]. We shine right-hand circular polarized light on a bullseye antenna and detect in a polarization setting that is close to left-hand circular polarization, but deliberately not quite, letting through also a small fraction of right-handed circular polarization. In such a left-handed elliptical polarization channel, one would expect the radiation pattern to be an admixture of OAM 0 and 2. Figure 7(a) shows a bright concentric band for $k_r/k_0 \approx 0.2$ and a bright spot for forward scattering. The bright band originates from diffraction of surface plasmons off the bullseye antenna. We detect some forward scattering due to the deliberate slight mismatch in the orthogonal polarizer setting. We observe two local minima through which we draw a dashed white line as a guide for the eye. Figure 7(c) shows that this pair of minima rotate around the optical axis as the camera is displaced from focus (example shown: $\Delta z = 17$ cm). For this example, the local minima are rotated by 13 degrees counter-clockwise, as indicated by the white dashed line. Both the observation of an anti-clockwise rotation and the persistence of the local minima suggest they should come with two phase singularities of positive topological charge. Figure 7(b) shows the retrieved phase profile. We indeed observe a phase singularity for both angles at which we observed a local minimum of the intensity. The topological charge of both phase singularities is +1, which is consistent with the observed anti-clockwise rotation of the line that connects both minima. To rationalize this behavior, we note that a simple analysis of a superposition of two Laguerre-Gaussian beams, one of OAM 0, and one of OAM 2, reveals a similar rotation, where the typical length scale over which a rotation can be observed is determined by the Rayleigh range z_R of the beam. For our experiment, we approximate the waist from the camera image as $w_0 = 3 \cdot 10^2$ μm (1/e-distance calculated from
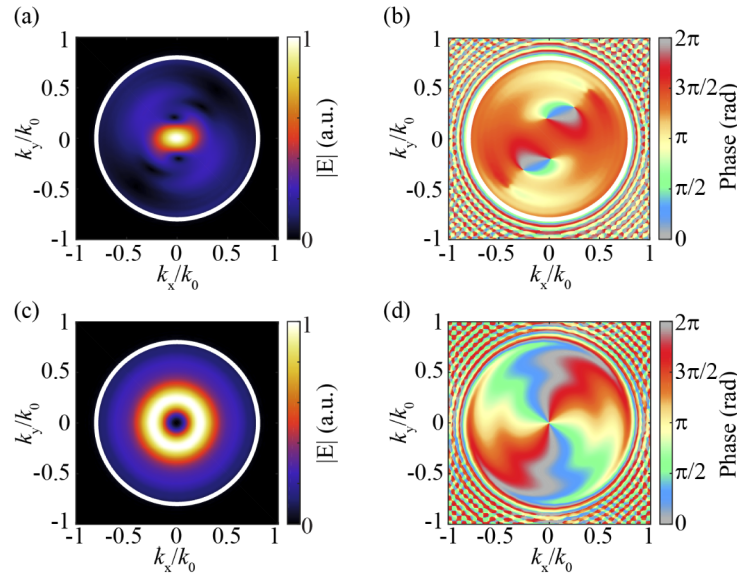
Fig. 6. Simulated scattered fields. (a,b) Amplitude (a) and phase (b) of the scattered field in the plane $\Delta z = 0$ cm, for a vertically polarized plane wave ($\lambda = 632.8$ nm) scattering from bullseye antenna and left-hand circular polarized light is analyzed. (c,d) Amplitude (c) and phase (d) of the scattered field in the plane $\Delta z = 0$ cm, for a right-hand circular polarized plane wave ($\lambda = 632.8$ nm) scattering from bullseye antenna and left-hand circular polarized light is analyzed.

the location of the maximum amplitude), so we would expect a rotation of $\arctan\left(\frac{\Delta z}{z_R}\right) = 2 \cdot 10^1$ degrees. This estimate is reasonably close to the experimental observation, given the approximate nature of the calculation.

Figures 7(a) and (b) versus (d) and (e) allows a comparison between propagation-based phase retrieval and digital off-axis holography for this more challenging case. To facilitate the reconstruction for this case, we started the algorithm with an initial phase gradient corresponding to OAM = 2, plus random noise, based on the expected selection rule due to Gorodetski *et al*. [12]. It is evident from Fig. 7(b) that the algorithm correctly reconstructs the beam as a superposition of OAM is 0 and OAM 2, meaning that the charge +2 singularity in the initial guess is split in two phase singularities with a topological charge of +1. The comparison with off-axis holography (Figs. 7(d) and (e)) confirms that our algorithm also works for chiral light. Figures 7(f) and (g) show the result of phase retrieval by defocused imaging when setting the detection polarizer to left-handed circular polarization, i.e., as orthogonal to the incident polarization as the quality of the waveplates allows. We observe that the two minima merge into a central dark spot, meaning that the forward scattering disappeared, as expected from symmetry arguments. The two phase singularities concomitantly approach each other and merge to a single topological charge of +2. Figure 7(h) shows the measured amplitude in the plane $\Delta z = 17$ cm. We do not observe a rotation as we have seen in Fig. 7(c), since the observed amplitude shows a high degree of circular symmetry. Figures 6(c) and (d) show the simulated electric field. They show excellent agreement with the experimental results.

With the results presented in Figs. 5 and 7 we have benchmarked and validated phase retrieval against off-axis digital holography as a method for determining the phase in radiation patterns of single nano-objects for light that has a high degree of temporal coherence. This crucial first step
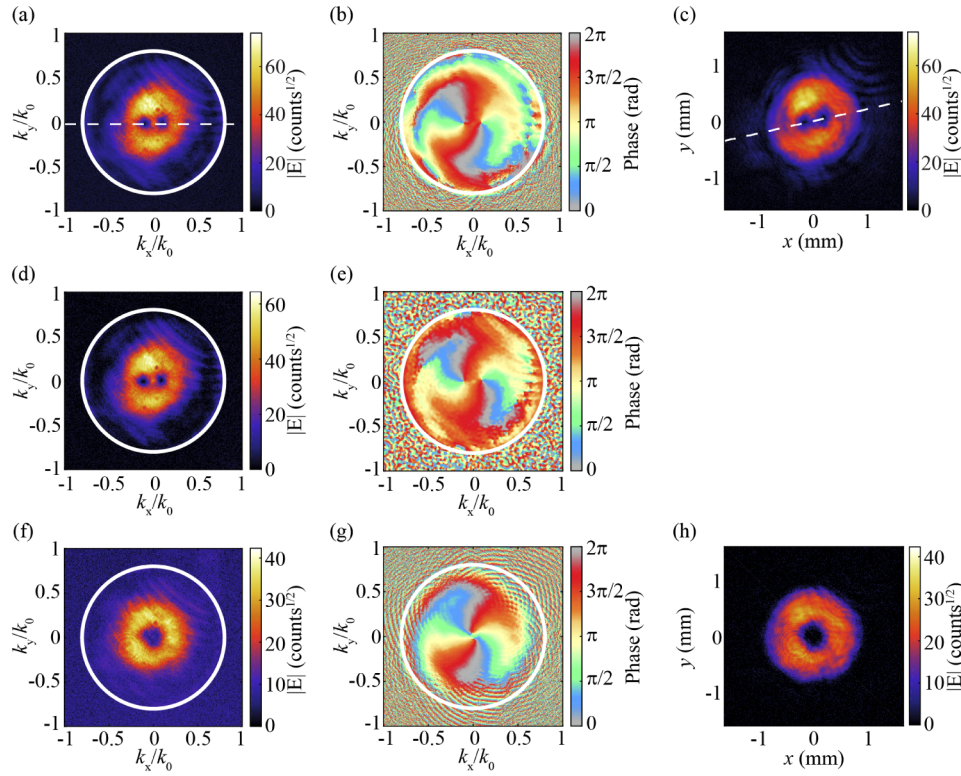
Fig. 7. Generation of orbital angular momentum by a bullseye antenna. (a-e) RHC polarized light (λ = 632.8 nm) is incident on the bullseye and we detect left-handed elliptically polarized light with an eccentricity close to $\pi/2$. (a) Measured electric field amplitude for defocused imaging experiment. Close to the origin, two local intensity minima are observed. A dashed line connects both local minima. (b) Phase of the electric field obtained by defocused imaging. Two phase singularities with topological charge of -1 are observed close to the origin. (c) Measured electric field amplitude in the plane Δz = 17 cm. The two local intensity minima are rotated by 13 degrees counterclockwise as compared to (a). (d,e) Electric field amplitude (d) and phase (e) measured with off-axis digital holography. Two phase singularities with topological charge of -1 can be observed close to the origin. (f-h) RHC polarized light (λ = 632.8 nm) is incident on the bullseye and we detect LHC polarized light. (f,g) Electric field amplitude (f) and phase (g) measured with defocused imaging. One phase singularity with topological charge of +2 is observed at the origin. (h) Measured electric field amplitude in the plane Δz = 17 cm.

brings us closer towards phase-resolved Fourier microscopy on partially temporally coherent light scattering by defocused imaging.

## 5. Phase-retrieval Fourier microscopy with partially temporally coherent light

In the remainder of this paper we investigate the potential of phase retrieval for light with a lower degree of temporal coherence, with bandwidths for which an interferometric reference experiment is not possible. To this end we use a supercontinuum laser which is spectrally filtered by an acousto-optic tunable filter (AOTF). We initially set the AOTF to a single channel with central wavelength λ_c = 632.8 nm identical to that of the HeNe laser. The spectral width of the filtered light is 1.5 nm, as limited by the AOTF. As a result of the short coherence length, in our

experimental setup we cannot perform off-axis digital holography. Vertically polarized light is incident on the bullseye antenna. We detect LHC polarized light. Figures 8(a) and (b) show the measured amplitude and the retrieved phase of the field, respectively. The data show the same features as observed in Figs. 5(a) and (b) for the HeNe laser. This evidences that phase retrieval by defocused imaging can be done in an optical setup where distances are beyond the coherence length of the light source. Due to differences in incident beam waist between the HeNe laser and the supercontinuum laser, we observe for supercontinuum laser experiments a brighter spot in the origin. To increase the dynamic range, we show the amplitude data on a logarithmic scale.

Having validated the algorithm for incoherent light at the HeNe wavelength, we now tune the AOTF to different wavelengths spread across the dispersion of the bullseye antenna response indicated by the horizontal dashed lines in Figs. 2(c) and (d). Figures 8(c) and (d) show the measured amplitude and retrieved phase of the field for $\lambda = 582.8$ nm, respectively. The retrieved phase shows two patches where we observe a similar variation of the phase as observed in Fig. 6(b), which comes with two phase singularities for each patch. The experimentally observed phase singularities are in agreement with simulations. Figures 8(e) and (f) show the measured amplitudes and retrieved phase of the field for $\lambda = 682.8$ nm, respectively. Both the radiation pattern and the phase profile show similarities with Figs. 8(a) and (b), respectively. The phase profile shows two patches, yet with a larger extent than the patches observed in Fig. 8(b).

Taken together, our results at 582.8 nm 632.8 nm and 682.8 nm, indicate that with phase retrieval we can determine the phasefronts in radiation patterns when using relatively incoherent incident light with a bandwidth of 1.5 nm, and that over the full span of 100 nm, the light scattering from the bullseye antenna continuously and significantly varies. Next, we study in how far phase retrieval by defocused imaging works when using a wide bandwidth illumination, as could be provided by a fluorescent emitter. To this end, we set the AOTF such that we have simultaneously three different channels of equal power $\lambda = \{582.8, 632.8, 682.8\}$ nm, thereby mimicking a 100 nm spectral width. We note that, while not fully sampling the spectrum of a specific fluorophore, matching a typical bandwidth using three wavelengths is suitable to test the limits of the phase-retrieval technique. After transmission by the bullseye antenna, the relative angle-integrated intensities for $\lambda = \{582.8, 632.8, 682.8\}$ nm are approximately 0.5, 1, 0.2, respectively. Figures 8(g) and (h) show the result of running the phase retrieval algorithm on this wide bandwidth data, setting the algorithm to use an assumed wavelength $\lambda = 632.8$ nm. Despite the large illumination bandwidth, the algorithm converges to a retrieved electric field amplitude and phase. The retrieved amplitude and phase profiles shown in Fig. 8(h) show significant resemblance to the measurements at just $\lambda = 632.8$ nm, which is the largest contributor to the data in terms of intensity. However, closer examination of the data also shows differences. The local intensity minima along the line $k_x/k_0 = 0$ are less deep than observed in Fig. 8(a) for $\lambda = 632.8$ nm only. This is a direct consequence of the different angular dispersion of the bullseye antenna for these wavelengths, since the three angular scattering patterns incoherently add up and, as can be seen from Figs. 8(a), (c), and (e) result in a less deep minimum. Similarly, the retrieved shape of the phase landscape differs. We attribute these differences to the fact that scattering is dispersive and different wavelengths show different phase profiles.

Our observations indicate that it is in principle procedurally possible to perform defocused imaging and phase retrieval on radiation from single nano-objects that is partially temporally coherent, with the 100 nm bandwidth in our experiment of the same order as the typical bandwidth of fluorophores and resonances in plasmonic systems. We expect two distinct mechanisms that determine the limitations on the physical significance of the retrieved phase for data taken with such spectrally broad illumination. The first limitation is the mode structure of the nanoantenna itself: for wavelengths chosen within the bandwidth of a single resonance that one probes one would expect nearly identical far field phasefronts, and therefore a high fidelity in retrieving such a field. Conversely, if one uses illumination with a spectrum over which the structure at
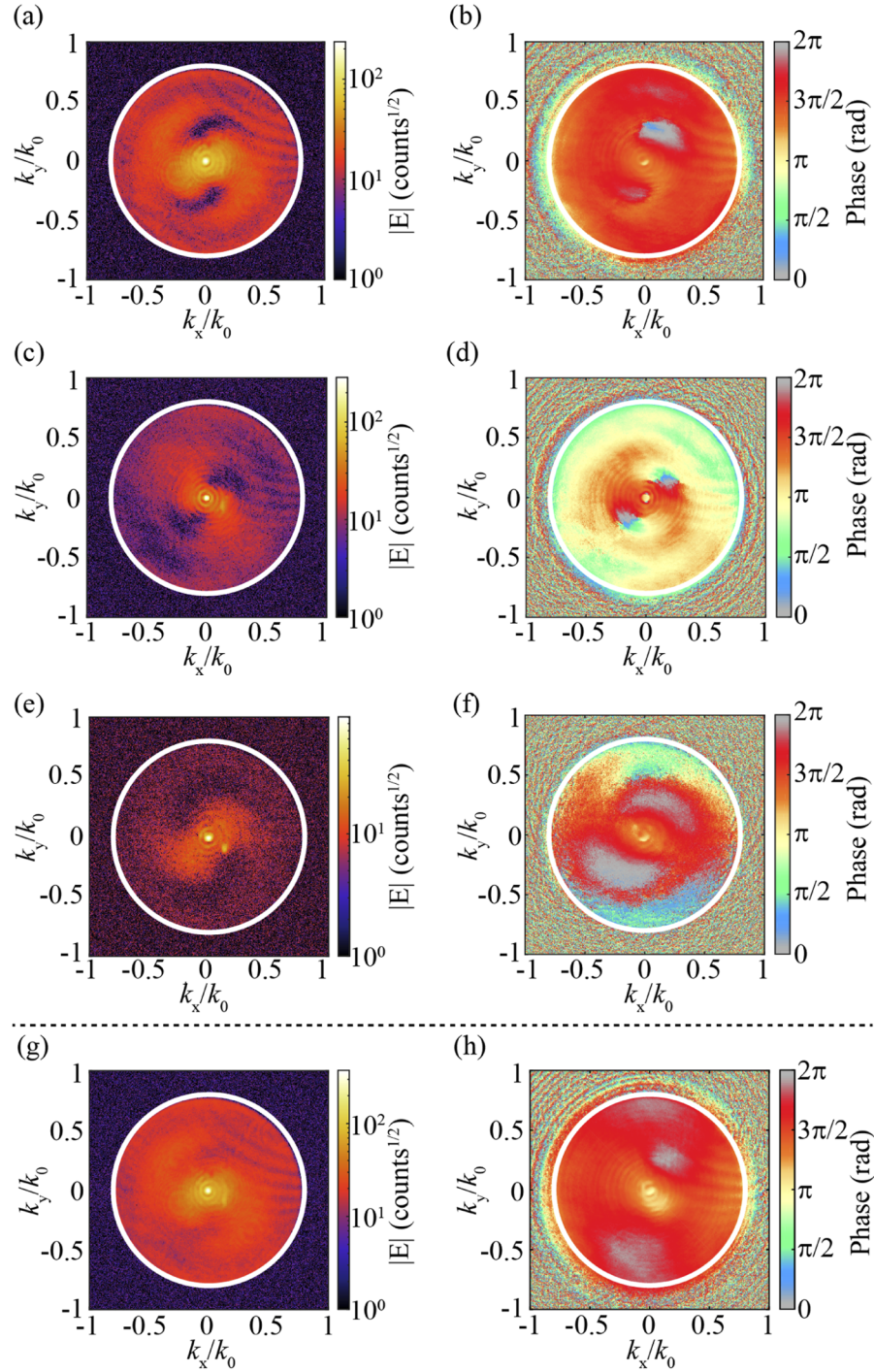
Fig. 8. Recovered electric far field from bullseye antenna illuminated by filtered super-continuum laser. Vertically polarized filtered supercontinuum laser is incident on bullseye antenna and left-hand circularly polarized light is analyzed. (a,c,e,g) Measured electric field amplitudes. (b,d,f,h) Retrieved phase from defocused imaging. (a,b) $\lambda = 632.8 \pm 0.5$ nm. (c,d) $\lambda = 582.8 \pm 0.5$ nm. (e,f) $\lambda = 682.8 \pm 0.5$ nm. (g,h) $\lambda = \{582.8, 632.8, 682.8\} \pm 0.5$ nm.

hand shows strong dispersion or multiple resonances, one would expect phase retrieval from the incoherent spectral average of defocused radiation patterns to not be very meaningful. A second mechanism that one could speculate to come into play is not due to the mode spectrum of the nanophotonic structure at hand, but due to the iterative phase retrieval algorithm which hinges on an assumed free-space propagator at an assumed central wavelength. We have verified that although the propagator used by the algorithm (cf. Eq. (1)) is dispersive, this dispersive nature hardly affects our algorithm. The propagator is not strongly affected by dispersion as long as $|\lambda - \lambda_c| \ll \frac{\Delta \lambda}{2}$, where

$$\Delta \lambda = \frac{4\pi^2}{\Delta z k_{\parallel,\text{max}}^2},\tag{2}$$

where Δz is the maximum displacement of the defocusing lens, and $k_{\parallel}$ is the highest spatial frequency in the radiation pattern. For an experimental setup such as presented in this work, this could be approximated by

$$\Delta \lambda \approx \frac{1}{1 - \text{NA}^2} \left(\frac{\lambda}{L_{\text{antenna}}}\right)^2 \left(\frac{f_{\text{obj}}}{f_{\text{FL}}}\right)^2 \frac{f_{\text{TL}}}{\Delta z_{\text{max}}} f_{\text{TL}}.\tag{3}$$

Since for our experiment the spatial frequency $k_{\parallel} \leq 2 \cdot 10^4 \ \text{m}^{-1}$, the phase deviates in the furthest plane $\Delta z = 25$ cm by less than 0.4, which is only 6% of 2π, even at the large 100 nm bandwidth of our trial. We conclude that one should expect iterative phase retrieval to decode phase information in radiation patterns of temporally incoherent sources to be meaningful as long as the optical response of the scattering object does not show much dispersion. We believe this result is very promising for phase retrieval even for decoding the phasefronts of fluorescence from individual emission centers coupled to nanoscale antennas.

6. Conclusion

To summarize, we have shown that phase-resolved Fourier imaging of single scattering objects can be done by applying an iterative phase retrieval algorithm on a set of defocused images. As long as the coherence time of the scattered light is longer than the coherence time of the resonant scattering object, this algorithm allows phase retrieval even for partially temporally coherent light. We believe that the ability to perform phase-resolved Fourier imaging on a single scattering object with partially temporally coherent light will be useful for the study of the near-to-farfield transformation of nanoscale antennas to which nanoscale emitters are coupled. In particular, this technique could be used to unravel from the emitted field how dipolar emitters become effectively multipolar due to coupling to plasmonic and dielectric antennas, Huygens particles, and so forth, how conversely chiral and multipolar transitions can be modified by nanoscale antennas, and the performance of, e.g., OAM-carrying single photon sources. While in this work we focused on temporal coherence, an important next step towards this goal would be to study in how far phase-resolved Fourier imaging is applicable to spatially incoherent sources, where nanophotonic structures can control the mutual coherence function [51–56].

7. Methods

Fabrication of multilayer stack A layer stack of 5 nm Cr and 200 nm Au was made by electron-beam evaporation. Au was deposited at a deposition rate of 5 Å/s and Cr at a rate of 1 Å/s. As a substrate we used a 170 μm thick glass cover slide.

Fabrication of bullseye antennas 30 keV Ga focused-ion beam milling of bullseye antennas was performed using serpentine scans at a current of 48 pA and a pixel dwell time of 1 μs. The grooves of the structure were made in 100 passes and the hole in 1000 passes.

Microscope It is important for phase-retrieval Fourier microscopy that the BFP of the Fourier lens spatially overlaps with the front-focal plane (FFP) of the tube lens, a condition that was not

met in our recent work on off-axis holography Fourier microscopy [28]. When this condition is not met, a plane wave in the BFP of the objective is transformed into a spherical wave at BFP of the TL. As a consequence, several concentric circles are seen in the phase profile.

Funding

Acknowledgements

Disclosures

The authors declare no conflicts of interest.

References

1. N. Yu, P. Genevet, M. A. Kats, F. Aieta, J.-P. Tetienne, F. Capasso, and Z. Gaburro, "Light Propagation with Phase Reflection and Refraction," Science **334**(6054), 333–337 (2011).
2. N. Yu and F. Capasso, "Flat optics with designer metasurfaces," Nat. Mater. **13**(2), 139–150 (2014).
3. A. Arbabi, Y. Horie, M. Bagheri, and A. Faraon, "Dielectric metasurfaces for complete control of phase and polarization with subwavelength spatial resolution and high transmission," Nat. Nanotechnol. **10**(11), 937–943 (2015).
4. J. A. Fan, C. Wu, K. Bao, J. Bao, R. Bardhan, N. J. Halas, V. N. Manoharan, P. Nordlander, G. Shvets, and F. Capasso, "Self-assembled plasmonic nanoparticle clusters," Science **328**(5982), 1135–1138 (2010).
5. M. Hentschel, M. Saliba, R. Vogelgesang, H. Giessen, A. P. Alivisatos, and N. Liu, "Transition from isolated to collective modes in plasmonic oligomers," Nano Lett. **10**(7), 2721–2726 (2010).
6. A. E. Miroshnichenko and Y. S. Kivshar, "Fano resonances in all-dielectric oligomers," Nano Lett. **12**(12), 6459–6463 (2012).
7. E. M. Hicks, S. Zou, G. C. Schatz, K. G. Spears, R. P. Van Duyne, L. Gunnarsson, T. Rindzevicius, B. Kasemo, and M. Käll, "Controlling plasmon line shapes through diffractive coupling in linear arrays of cylindrical nanoparticles fabricated by electron beam lithography," Nano Lett. **5**(6), 1065–1070 (2005).
8. V. Giannini, G. Vecchi, and J. Gómez Rivas, "Lighting up multipolar surface plasmon polaritons by collective resonances in arrays of nanoantennas," Phys. Rev. Lett. **105**(26), 266801 (2010).
9. M. Limonov, M. Rybin, A. Poddubny, and Y. Kivshar, "Fano resonances in photonics," Nat. Photonics **11**(9), 543–554 (2017).
10. M. Hentschel, M. Schäferling, X. Duan, H. Giessen, and N. Liu, "Chiral plasmonics," Sci. Adv. **3**(5), e1602735 (2017).
11. L. V. Poulikakos, P. Thureja, A. Stollmann, E. De Leo, and D. J. Norris, "Chiral light design and detection inspired by optical antenna theory," Nano Lett. **18**(8), 4633–4640 (2018).
12. Y. Gorodetski, A. Drezet, C. Genet, and T. W. Ebbesen, "Generating far-field orbital angular momenta from near-field optical chirality," Phys. Rev. Lett. **110**(20), 203906 (2013).
13. E. Karimi, S. A. Schulz, I. De Leon, H. Qassim, J. Upham, and R. W. Boyd, "Generating optical orbital angular momentum at visible wavelengths using a plasmonic metasurface," Light: Sci. Appl. **3**(5), e167 (2014).
14. Y.-H. Chen, L. Huang, L. Gan, and Z.-Y. Li, "Wavefront shaping of infrared light through a subwavelength hole," Light: Sci. Appl. **1**(8), e26 (2012).
15. K. Y. Bliokh, F. Rodríguez-Fortuno, F. Nori, and A. V. Zayats, "Spin-orbit interactions of light," Nat. Photonics **9**(12), 796–808 (2015).
16. A. F. Koenderink, "Single-photon nanoantennas," ACS Photonics **4**(4), 710–722 (2017).

17. A. G. Curto, G. Volpe, T. H. Taminiau, M. P. Kreuzer, R. Quidant, and N. F. van Hulst, "Unidirectional emission of a quantum dot coupled to a nanoantenna," Science **329**(5994), 930–933 (2010).

18. T. Coenen, E. J. R. Vesseur, A. Polman, and A. F. Koenderink, "Directional emission from plasmonic yagi-uda antennas probed by angle-resolved cathodoluminescence spectroscopy," Nano Lett. **11**(9), 3779–3784 (2011).

19. G. Lozano, D. J. Louwers, S. R. Rodraguez, S. Murai, O. T. Jansen, M. A. Verschuuren, and J. G. Rivas, "Plasmonics for solid-state lighting: enhanced excitation and directional emission of highly efficient light sources," Light: Sci. Appl. **2**(5), e66 (2013).

20. W. Wang, M. Ramezani, A. Väkeväinen, P. Törmä, J. Rivas, and T. Odom, "The rich photonic world of plasmonic nanoparticle arrays," Mater. Today **21**(3), 303–314 (2017).

21. H. Aouani, O. Mahboub, N. Bonod, E. Devaux, E. Popov, H. Rigneault, T. W. Ebbesen, and J. Wenger, "Bright unidirectional fluorescence emission of molecules in a nanoaperture with plasmonic corrugations," Nano Lett. **11**(2), 637–644 (2011).

22. H. Aouani, O. Mahboub, E. Devaux, H. Rigneault, T. W. Ebbesen, and J. Wenger, "Plasmonic antennas for directional sorting of fluorescence emission," Nano Lett. **11**(6), 2400–2406 (2011).

23. M. Lieb, J. Zavislan, and L. Novotny, "Single-molecule orientations determined by direct emission pattern imaging," J. Opt. Soc. Am. B **21**(6), 1210–1215 (2004).

24. I. Sersic, C. Tuambilangana, and A. F. Koenderink, "Fourier microscopy of single plasmonic scatterers," New J. Phys. **13**(8), 083019 (2011).

25. J. Kurvits, M. Jiang, and R. Zia, "Comparative analysis of imaging configurations and objectives for fourier microscopy," J. Opt. Soc. Am. A **32**(11), 2082–2092 (2015).

26. C. I. Osorio, A. Mohtashami, and A. F. Koenderink, "K-space polarimetry of bullseye plasmon antennas," Sci. Rep. **5**(1), 9966 (2015).

27. A. Mohtashami, C. I. Osorio, and A. F. Koenderink, "Angle-resolved polarimetry of antenna-mediated fluorescence," Phys. Rev. Appl. **4**(5), 054014 (2015).

28. R. Röhrich, C. Hoekmeijer, C. I. Osorio, and A. F. Koenderink, "Quantifying single plasmonic nanostructure far-fields with interferometric and polarimetric k-space microscopy," Light: Sci. Appl. **7**(1), 65 (2018).

29. J. Leach, M. J. Padgett, S. M. Barnett, S. Franke-Arnold, and J. Courtial, "Measuring the orbital angular momentum of a single photon," Phys. Rev. Lett. **88**(25), 257901 (2002).

30. N. Streibl, "Phase imaging by the transport equation of intensity," Opt. Commun. **49**(1), 6–10 (1984).

31. L. J. Allen and M. P. Oxley, "Phase retrieval from series of images obtained by defocus variation," Opt. Commun. **199**(1-4), 65–75 (2001).

32. T. E. Gureyev, A. Roberts, and K. A. Nugent, "Partially coherent fields, the transport-of-intensity equation, and phase uniqueness," J. Opt. Soc. Am. A **12**(9), 1942–1946 (1995).

33. D. Paganin and K. A. Nugent, "Noninterferometric phase imaging with partially coherent light," Phys. Rev. Lett. **80**(12), 2586–2589 (1998).

34. L. J. Allen, H. M. L. Faulkner, K. A. Nugent, M. P. Oxley, and D. Paganin, "Phase retrieval from images in the presence of first-order vortices," Phys. Rev. E **63**(3), 037602 (2001).

35. A. Lubk, G. Guzzinati, F. Börrnert, and J. Verbeeck, "Transport of intensity phase retrieval of arbitrary wave fields including vortices," Phys. Rev. Lett. **111**(17), 173902 (2013).

36. T. Tahara, X. Quan, R. Otani, Y. Takaki, and O. Matoba, "Digital holography and its multidimensional imaging applications: A review," Microscopy **67**(2), 55–67 (2018).

37. T. Slabý, P. Kolman, Z. Dostál, M. Antoš, M. Lošťák, and R. Chmelík, "Off-axis setup taking full advantage of incoherent illumination in coherence-controlled holographic microscope," Opt. Express **21**(12), 14747–14762 (2013).

38. J.-P. Liu, T. Tahara, Y. Hayasaki, and T.-C. Poon, "Incoherent digital holography: A review," Appl. Sci. **8**(1), 143 (2018).

39. B. W. Schilling, T.-C. Poon, G. Indebetouw, B. Storrie, K. Shinoda, Y. Suzuki, and M. H. Wu, "Three-dimensional holographic fluorescence microscopy," Opt. Lett. **22**(19), 1506–1508 (1997).

40. J. Rosen and G. Brooker, "Digital spatially incoherent fresnel holography," Opt. Lett. **32**(8), 912–914 (2007).

41. C. Jang, J. Kim, D. C. Clark, S. Lee, B. Lee, and M. K. Kim, "Holographic fluorescence microscopy with incoherent digital holographic adaptive optics," J. Biomed. Opt. **20**(11), 111204 (2015).

42. M. R. Teague, "Deterministic phase retrieval: a green's function solution," J. Opt. Soc. Am. **73**(11), 1434–1441 (1983).

43. P. Thibault and A. Menzel, "Reconstructing state mixtures from diffraction measurements," Nature **494**(7435), 68–71 (2013).

44. N. J. Schilder, H. Agrawal, E. C. Garnett, and A. Polman, "Phase-Resolved Surface Plasmon Scattering Probed by Cathodoluminescence Holography," ACS Photonics **7**(6), 1476–1482 (2020).

45. D. L. Misell, "A method for the solution of the phase problem in electron microscopy," J. Phys. D: Appl. Phys. **6**(1), L6–L9 (1973).

46. H. J. Lezec, A. Degiron, E. Devaux, R. A. Linke, L. Martin-Moreno, F. J. Garcia-Vidal, and T. W. Ebbesen, "Beaming light from a subwavelength aperture," Science **297**(5582), 820–822 (2002).

47. F. J. Garcia-Vidal, L. Martin-Moreno, T. W. Ebbesen, and L. Kuipers, "Light passing through subwavelength apertures," Rev. Mod. Phys. **82**(1), 729–787 (2010).

48. N. Bonod, E. Popov, and M. Nevière, "Differential theory of diffraction by finite cylindrical objects," J. Opt. Soc. Am. A **22**(3), 481–490 (2005).
49. P. B. Johnson and R. W. Christy, "Optical Constants of the Noble Metals," Phys. Rev. B **6**(12), 4370–4379 (1972).
50. Y. Lim, S.-Y. Lee, and B. Lee, "Transflective digital holographic microscopy and its use for probing plasmonic light beaming," Opt. Express **19**(6), 5202–5212 (2011).
51. C. H. Gan, G. Gbur, and T. D. Visser, "Surface plasmons modulate the spatial coherence of light in Young's interference experiment," Phys. Rev. Lett. **98**(4), 043908 (2007).
52. N. Kuzmin, G. W. 't Hooft, E. R. Eliel, G. Gbur, H. F. Schouten, and T. D. Visser, "Enhancement of spatial coherence by surface plasmons," Opt. Lett. **32**(5), 445–447 (2007).
53. C. H. Gan, Y. Gu, T. D. Visser, and G. Gbur, "Coherence Converting Plasmonic Hole Arrays," Plasmonics **7**(2), 313–322 (2012).
54. T. Saastamoinen and H. Lajunen, "Increase of spatial coherence by subwavelength metallic gratings," Opt. Lett. **38**(23), 5000–5003 (2013).
55. S. Divitt, M. Frimmer, T. D. Visser, and L. Novotny, "Modulation of optical spatial coherence by surface plasmon polaritons," Opt. Lett. **41**(13), 3094–3097 (2016).
56. D. Li and D. Pacifici, "Strong amplitude and phase modulation of optical spatial coherence with surface plasmon polaritons," Sci. Adv. **3**(10), e1700133 (2017).